

Pseudo Temperature Independent Paramagnetism in $\text{Co}_2\text{Si}_5\text{N}_8$ Nitridosilicate

Cordula Braun, Liuda Mereacre, Tobias Stürzer, and Björn Schwarz*

Herein, the synthesis of $\text{Co}_2\text{Si}_5\text{N}_8$ nitridosilicate from $\alpha\text{-Ca}_2\text{Si}_5\text{N}_8$ by ion exchange is described. The monoclinic $\text{Co}_2\text{Si}_5\text{N}_8$ structure (space group Cc) is compared with those of the related nitridosilicates $\text{Ca}_2\text{Si}_5\text{N}_8$ and $\text{Fe}_2\text{Si}_5\text{N}_8$ its magnetic properties are profoundly investigated. Most interestingly, polycrystalline $\text{Co}_2\text{Si}_5\text{N}_8$ exhibits a quasi-temperature-independent paramagnetic susceptibility of about $6 \times 10^{-3} \text{ cm}^3 \text{ mol}^{-1}$ over a wide temperature range from 100 to 600 K. Two different magnetic models based on a phenomenological Hamiltonian that takes into account magnetic exchange coupling, crystal-field interactions, and Zeeman effects within the framework of an angular momentum basis set are refined to the experimental susceptibility datasets. The results of the refinements point to the realization of a pseudo temperature independent paramagnetism for $\text{Co}_2\text{Si}_5\text{N}_8$ that results from a near-perfect cancellation of temperature-dependent contributions to the susceptibility depending delicately on the mixing of ion levels in the electronic states, their relative energies, and the magnetic coupling between them. Additionally, performed direct current field scan, alternating current susceptibility, and heat capacity measurements complete the magnetic characterization and facilitate the identification of impurity phase contributions.

is based on an ion exchange taking place in a salt melt with a presynthesized $\text{M}_2\text{Si}_5\text{N}_8$ compound. While the counter ions are exchanged via migration channels, the highly covalent Si–N bonds are preserved proving that even the rigid nitridosilicate structure is able to adapt to the special requirements of the different cation sizes. $\text{Co}_2\text{Si}_5\text{N}_8$ has been once mentioned in the literature^[23,25] to have been synthesized, but there has never been a detailed description of this compound and its properties. Another attempt in the literature^[26] started from Co metal and silicon diimide and yielded hexagonal Si_3N_4 microtubes filled with intermetallic Co/Si compounds instead of Co nitridosilicates.

In the following, an introduction to temperature-independent paramagnetism (TIP) is given, a phenomenon that has also been observed for $\text{Co}_2\text{Si}_5\text{N}_8$ in this work. A discussion in how far a “real” or a pseudo-TIP is present here constitutes a major part of this work. More detailed

information about TIP can be found in refs. [27–31], for instance. Any energy-level E_i of an atom can be expressed as a power series in the applied magnetic field H according to $E_i = E_i^{(0)} + E_i^{(1)}H + E_i^{(2)}H^2 + \dots$, with the unperturbed and the first- and second-order Zeeman (ZEE) effects, respectively. The first-order ZEE effect can be thought to stem from permanent magnetic moments of a certain energy state with linear dependence of energy on the magnetic field. The second-order ZEE effect takes into account that the perturbed states are not any longer the pure states of the unperturbed free ion, but mixtures of these. Assuming that the thermal energy $k_B T$ is much greater than all energy terms containing H , the molar susceptibility can be written as

$$\chi_m = N \frac{\sum [E_i^{(1)2} / kT - 2E_i^{(2)}] e^{-(E_i^{(0)}/k_B T)}}{\sum e^{-(E_i^{(0)}/k_B T)}}. \quad (1)$$


In the case that the excited energy levels are either much smaller or much larger than $k_B T$ this expression can be simplified to $\chi'_m = C/T + \text{TIP}$. If the system only possesses a first-order ZEE effect (all $E_i^{(2)}$ and higher terms are zero), the Curie law describes the inverse temperature dependence of the susceptibility with the Curie constant C and temperature T . If, on the other side, when $E_i^{(1)} = 0$, i.e., only second-order ZEE effects contribute, a TIP would be realized that is also

1. Introduction

Highly condensed nitridosilicates, consisting of polymeric Si–N networks, possess extraordinary chemical and thermal stability and have proven to be excellent host structures for phosphor-converted white light-emitting diodes, when doped with, e.g., Eu^{2+} .^[1–21] Not long ago, a novel synthesis access to open-shell nitridosilicates was presented by Bielec et al.^[22–24] This approach

C. Braun, L. Mereacre, B. Schwarz
Institute for Applied Materials (IAM)
Karlsruhe Institute of Technology (KIT)
Hermann-von-Helmholtz-Platz 1, 76344 Eggenstein-Leopoldshafen,
Germany
E-mail: bjoern.schwarz@kit.edu

T. Stürzer
Bruker AXS GmbH
Oestliche Rheinbrueckenstr. 49, 76187 Karlsruhe, Germany

 The ORCID identification number(s) for the author(s) of this article can be found under <https://doi.org/10.1002/pssb.202300480>.

© 2024 The Authors. physica status solidi (b) basic solid state physics published by Wiley-VCH GmbH. This is an open access article under the terms of the Creative Commons Attribution License, which permits use, distribution and reproduction in any medium, provided the original work is properly cited.

DOI: 10.1002/pssb.202300480

known as Van Vleck high-frequency, residual, or feeble paramagnetism. TIP can be found for different systems that have in common to exhibit a nonmagnetic ground state (GS). Trivalent Eu ions, as present for instance in EuBO_3 , have a 7F_0 ($S = 3$, $L = 3$, $J = 0$) nonmagnetic GS that is separated from a first excited 7F_1 state by the energy $E_1 = \lambda$, with the spin-orbit (SO) coupling constant $\lambda \approx 471$ K. As a consequence, a TIP of the order of $4.9 \times 10^{-3} \text{ cm}^3 \text{ mol}^{-1}$ can be observed up to about 100 K.^[32] Tetrahedrally coordinated ionic complexes of transition metals like Mn^{7+} in permanganate MnO_4^- , Cr^{6+} in chromium trioxide, V^{5+} in vanadium pentoxide, and Ti^{4+} in titanium dioxide, respectively, all exhibit feeble paramagnetism.^[33] For example, the MnO_4^- possesses a 1A_1 GS with electronic configuration [...] $(t_1)^6$ and $S = L = 0$. The strongest contribution to the TIP cannot be ascribed to lowest energy excitations from the highest occupied molecular orbital to the triplet states $(t_1)^5 2e$ or $(1t_2)^5 3t_2$, but to an excitation from the lowest molecular orbital to the $(1t_2)^5 2e$ triplet state. In total, the TIP contributes here with about $63 \times 10^{-6} \text{ cm}^3 \text{ mol}^{-1}$.

Besides the SO coupling of the trivalent Eu ion that leads to the $J = 0$ GS and the d^0 metal ion electron configuration of the mainly ionic transition metal complexes with a $S = L = 0$ GS, also ligand fields can cause a (weak) TIP behavior for a large number of transition metal ions with partially filled d shell.^[34,35] Restricting the considerations to Co here, Co^{2+} with $[\text{Ar}]3d^7$ has a 4F GS as free ion. A tetrahedral T_4 ligand field causes this state to split into a 4A_2 ground term and the excited 4T_2 and 4T_1 terms. In the 4A_2 ground term, the orbital momentum from the d electrons is quenched, but second-order SO coupling effects mix the excited states into this ground term and as a consequence there is a small temperature-independent contribution to the susceptibility from the second-order ZEE effect. This contribution is, however, masked by the much stronger Curie contribution from the spin moment. A Co^{3+} with $[\text{Ar}]3d^6$ electronic configuration has a 5D GS as free ion. A strong octahedral O_h ligand field causes this state to split into a 1A_1 ground term and an excited 5T_2 term. As the ground term does neither contain a spin nor an orbital contribution, the temperature-independent contribution to the susceptibility from the second-order ZEE effect is more clearly observable. So far, only single-site systems have been considered. For the $\text{Co}_2\text{Si}_5\text{N}_8$ nitridosilicate investigated in this work, the TIP behavior as reported for a dinuclear Co^{2+} complex $[\text{Co}_2\text{PdCl}_2(\text{dpa})_4]$ is of importance.^[36] This heterotrimetallic complex shows a TIP of about $10 \times 10^{-3} \text{ cm}^3 \text{ mol}^{-1}$ over a broad temperature range up to 300 K and is 100 times larger than common values in mononuclear complexes.^[37] It is explained by the quenching of magnetic moments in thermally populated levels by a strong antiferromagnetic exchange interaction. Within this context, the large TIP of $0.536 \times 10^{-3} \text{ cm}^3 \text{ mol}^{-1}$ between 1 and 1000 K as reported for PuO_2 is also of interest. Based on complete active space (CAS) wave function results, Gendron and Autschbach^[38] suggest to consider this as a pseudo-TIP, which is a near-perfect cancellation of temperature-dependent contributions to the susceptibility that depends delicately on the mixing of ion levels in the electronic states, their relative energies, and the magnetic coupling between them.

2. Results and Discussion

2.1. Structure

The crystal structure of $\text{Co}_2\text{Si}_5\text{N}_8$ was determined and refined based on powder X-ray diffraction (PXRD) data in space group Cc (no. 9 in the international tables of crystallography) with $a = 14.1048(5) \text{ \AA}$, $b = 5.28414(18) \text{ \AA}$, $c = 9.5447(3) \text{ \AA}$, $\beta = 110.54^\circ$, $V = 666.14(4) \text{ \AA}^3$, and $Z = 4$. The observed and calculated PXRD pattern as well as their difference curve after Rietveld refinement^[39] is shown in **Figure 1**. Crystallographic data and details of the Rietveld refinement are listed in Table S1, Supporting Information. Selected bond lengths and angles of $\text{Co}_2\text{Si}_5\text{N}_8$ are summarized in Table S2 and S3, Supporting Information, respectively, and the occupied Wyckoff sites and refined atomic coordinates are listed in Table S4, Supporting Information. Estimated standard deviations are calculated according to ref. [40].

Additional information about the Rietveld refinement to the XRD pattern, especially with respect to details of the Co site occupation, and to potential additional impurity phases, can be found in the last section of the Supporting Information. In short, the observed intensities of the XRD pattern can well be explained by the occupation of the crystallographic sites according to the nominal composition $\text{Co}_2\text{Si}_5\text{N}_8$. Depending also on the specific thermal displacement factors that are ascribed to the two Co sites and that exhibit a high correlation with the site occupation, only a small, nonsignificant partial occupation by Ca and/or an even smaller partial occupation by vacancies can be attested. Further, only very small traces of a residual CaCl_2 phase that has not been washed away completely after synthesis can be observed.

The results of the scanning electron microscopy (SEM)-energy dispersive X-ray spectroscopy (EDX) analysis of $\text{Co}_2\text{Si}_5\text{N}_8$ are listed in Table S5, Supporting Information. The used emission line energies for the elements N, Si, Ca, and Co differ considerably from each other and as a consequence also the absorption

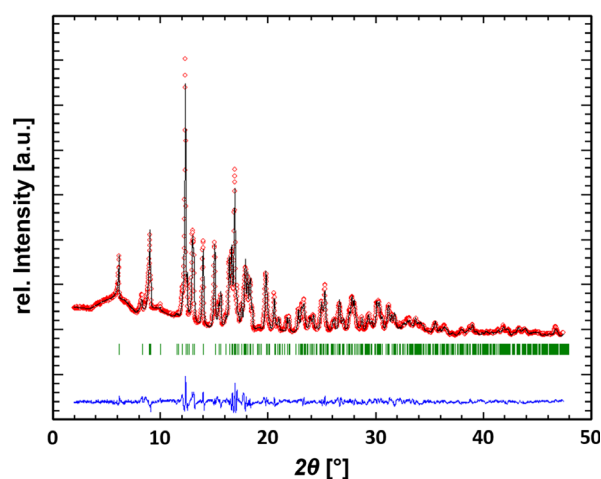


Figure 1. Observed (red) and calculated (black) PXRD patterns as well as their difference curve (blue) after Rietveld refinement ($\lambda = 0.709026 \text{ \AA}$). The green vertical ticks indicate the positions of the Bragg reflections of the monoclinic $\text{Co}_2\text{Si}_5\text{N}_8$ structure.

coefficients for the emitted radiation are very different. From the measured total net counts for the different elements, the elemental concentrations are quantitatively determined by considering the atomic number (Z), the absorption (A), and the fluorescence excitation (F) effect (shortly called ZAF correction). Due to the very different emission line energies, the obtained elemental concentrations should be considered critically because they might not reflect the actual concentrations. This holds particularly for a powder sample with poor defined radiation pathways. For instance, the Si:N ratio of the investigated $\text{Co}_2\text{Si}_5\text{N}_8$ sample can reasonably be assumed to be 5:8, but the SEM-EDX returns a ratio of $\approx 1:1$, i.e., the determined N-concentration is too small. Also, the ratio of (Co + Ca) to Si, and to N, does not reflect what has reliably been obtained by the Rietveld analysis. However, the obtained ratio of the total net count of Ca compared to Co is only 1.3% even though the used Ca K energy of 3692 eV is much higher than the Co L energy of 776 eV. And also the ratio of the determined atomic concentration of Ca-to-Co is only about 2.7%. These low Ca-to-Co ratios as obtained by the SEM-EDX analysis indicate that only a negligible small amount of Ca is still present in the sample and might partially occupy the Co sites in agreement with the results from Rietveld refinement.

The structure type $\text{M}_2\text{Si}_5\text{N}_8$ ($\text{M}=\text{Ca}, \text{Sr}, \text{Ba}$)^[41,42] is made up from vertex sharing SiN_4 -tetrahedra. These tetrahedra form corrugated layers consisting of highly condensed dreier-rings,^[43] which are interconnected by further SiN_4 -tetrahedra. The SiN_4 -tetrahedra within the layers build up configuration pattern generated by vertices pointing up and down. The pattern and their tilting angles are different for each modification and are indirectly influenced by the size of the M^{2+} ions situated between these layers. The structure of nitridosilicate in general^[4,5,44] and the structure of $\text{Ca}_2\text{Si}_5\text{N}_8$ ^[5,41] have already been described in detail in the literature, and that of $\text{Co}_2\text{Si}_5\text{N}_8$ and $\text{Fe}_2\text{Si}_5\text{N}_8$ ^[25] have also been published. Therefore, only a short comparative description of how the size of the inserted cation affects structural details, as distances between the tetrahedra and the pattern of the tetrahedra layers, will be given in this work.

Figure S1, Supporting Information, shows a comparison of the structures of $\text{Ca}_2\text{Si}_5\text{N}_8$ ^[41], $\text{Co}_2\text{Si}_5\text{N}_8$ and $\text{Fe}_2\text{Si}_5\text{N}_8$.^[25] Here, it becomes visible that the distances between the SiN_4 -tetrahedra differ significantly and can be correlated with the cation size. Ca^{2+} is the biggest one of the three with a cation radius of 1.12 Å and has an upper distance between the tetrahedra of 5.15 Å and a lower one of 5.08 Å (marked with red arrows in Figure S1a, Supporting Information). In $\text{Fe}_2\text{Si}_5\text{N}_8$,^[25] it is apparent that the distance is already significantly smaller as Fe^{2+} (0.63 Å) is considerably smaller than Ca^{2+} (upper distance: 4.89 Å; lower distance: 4.86 Å, marked with orange arrows in Figure S1c, Supporting Information). Co^{2+} has the smallest ion radius with 0.56 Å, which leads to more tilted tetrahedra and an even smaller distance (upper distance: 4.79 Å; lower distance: 4.87 Å, marked with violet arrows in Figure S1b, Supporting Information). Having a look at the corrugated tetrahedra pattern, this feature continues. The smallest cation, Co^{2+} in $\text{Co}_2\text{Si}_5\text{N}_8$, has the smallest tilting angle (108°) for the tetrahedra ($\text{Ca}_2\text{Si}_5\text{N}_8$:^[41] 111°; $\text{Fe}_2\text{Si}_5\text{N}_8$:^[25] 110°, see Figure S1, Supporting Information). As presented in Figure S2, Supporting

Information, the Co^{2+} ions are coordinated with 5 and 4 N-atoms, with coordination distances in the range of 1.88–2.88 Å, and these coordinations are different compared to those of $\text{Ca}_2\text{Si}_5\text{N}_8$ and $\text{Fe}_2\text{Si}_5\text{N}_8$, for instance. The Co^{2+} ions are located within these Sechser-ring^[43] channels (see Figure 2a). In Figure 2b, different views along the 100-direction are displayed. Here, the chain character of the Co^{2+} ions and their corresponding polyhedra becomes visible. Alternating units of Co1/Co2 -polyhedra convey the impression of a dimer character. These chains are interconnected via SiN_4 -tetrahedra having a very close distance of only 3.8 Å (see Figure 2c). Beyond that, Figure 2c illustrates a more detailed view including the Co–N distances and the Co–N–Co angles of the Co-polyhedra.

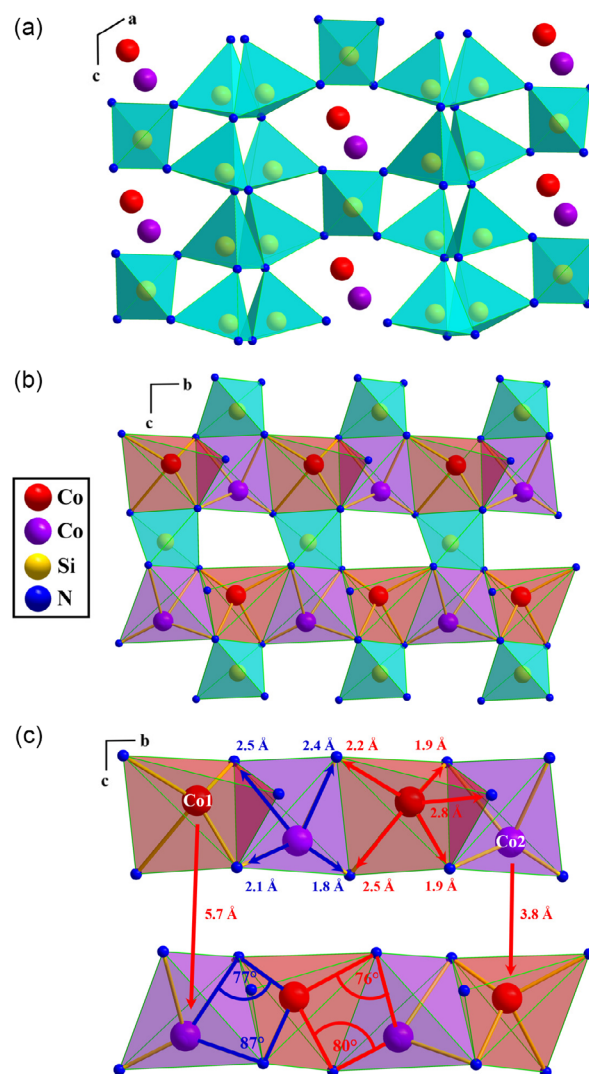


Figure 2. Sections of the crystallographic structure of $\text{Co}_2\text{Si}_5\text{N}_8$ a) in the 010-direction, b) in the 100-direction displaying the chain character of the Co polyhedra, and c) detailed view with distances and angles between the two different Co atoms.

2.2. Magnetic Characterization

2.2.1. Phenomenology of TIP

Figure 3a shows the magnetization versus field plots for various temperatures from 2 to 390 K. Interestingly, for temperatures above ≈ 100 K, these field scans exhibit a linear dependence of magnetization on magnetic field and they are all superimposed on each other. That means that a quasi-TIP is realized for $\text{Co}_2\text{Si}_5\text{N}_8$ above 100 K. The zero-field extrapolated magnetization obtained from a linear fit to the magnetization versus field plot from 70 to 60 kOe is a measure for the deviance from a pure linear progression. Figure S3, Supporting Information, illustrates that a clear deviation is present only for temperatures below 100 K and that above ≈ 100 K the deviations from a pure linear behavior are quasi-negligible. However, even these very weak nonlinearities of the magnetization versus field cause the susceptibility χ versus temperature curve measured at very low field of 0.25 kOe to be shifted slightly to higher values compared to those measured at 2.5 and 5 kOe, as shown in Figure 3b.

The low-temperature (<100 K) magnetic properties, with clear and strong deviations from a pure linear dependence of magnetization on the magnetic field, will be considered in detail in Section 2.2.3. First, the interesting TIP behavior as found for $\text{Co}_2\text{Si}_5\text{N}_8$ will be described in more detail. The high-temperature (HT) direct current (DC) magnetometry measurements reveal that a TIP behavior is present up to ≈ 600 K (see Figure S4, Supporting Information). Slightly above this temperature, some sort of reaction or decomposition of the $\text{Co}_2\text{Si}_5\text{N}_8$ main phase sets in and the susceptibility increases steeply. These changes are irreversible, i.e., the susceptibility at 300 K is about eight times higher after the HT experiment than before. This irreversibility is also apparent from the strongly modified magnetization versus field curve obtained at 300 K after the HT experiment with a strong deviation from a linear dependence due to a contribution from an easy saturating additional magnetic phase (Figure S4c, Supporting Information).

Figure 4a,b presents the χ , χT , and χ^{-1} versus temperature T plots, respectively, from 100 to 600 K that were obtained by combining the low-temperature with the HT susceptibility measurements. Over this broad range of temperatures, the

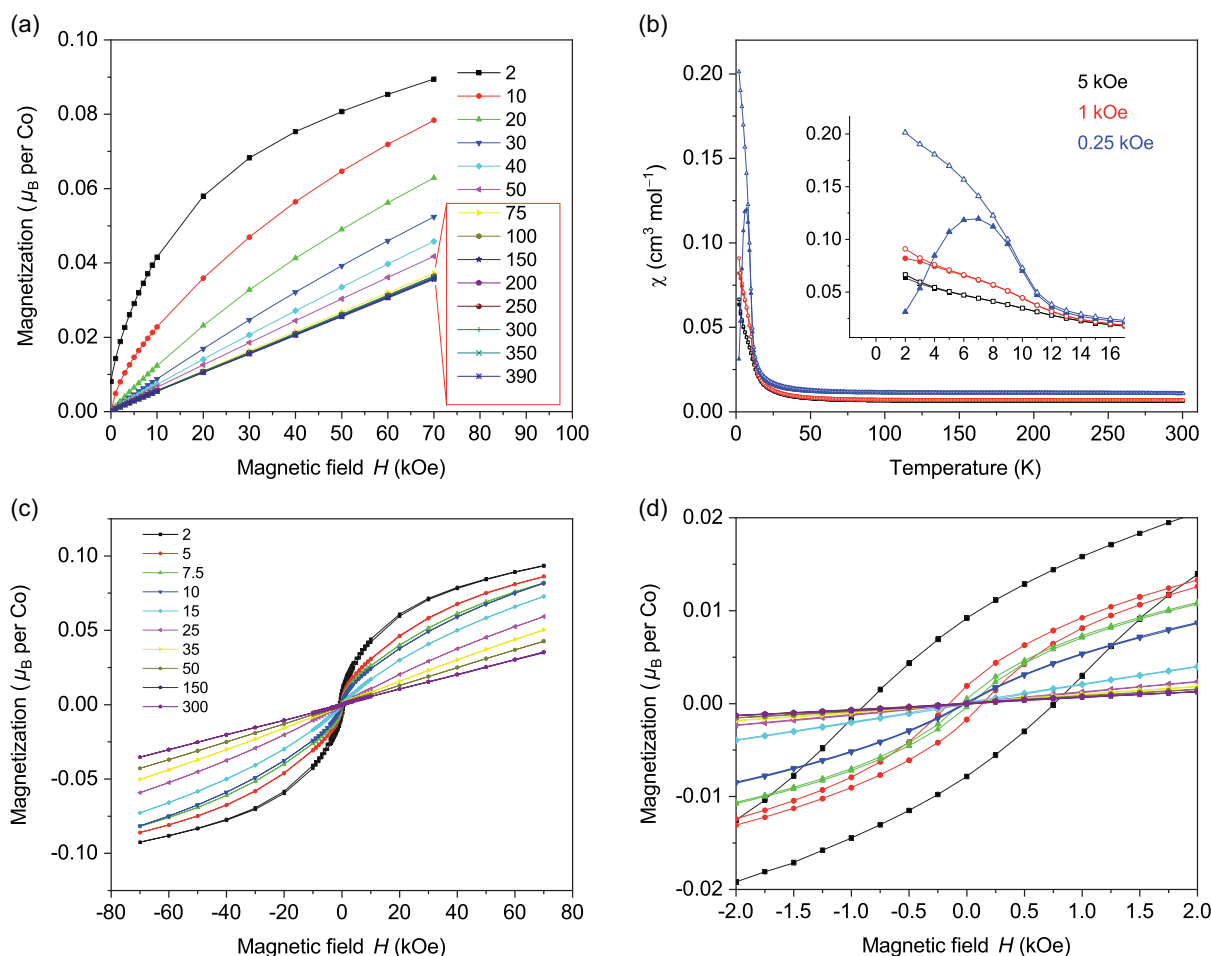


Figure 3. Experimental DC magnetic properties of $\text{Co}_2\text{Si}_5\text{N}_8$: a) magnetic field scans from 2 to 390 K for the positive field quadrant, b) susceptibility temperature scans for various magnetic fields obtained in ZFC (closed symbols) and FC (open symbols) mode, c) full loop magnetization versus field scans measured at various temperatures, and d) enlarged section of what is shown in (c). Error bars are smaller than symbols.

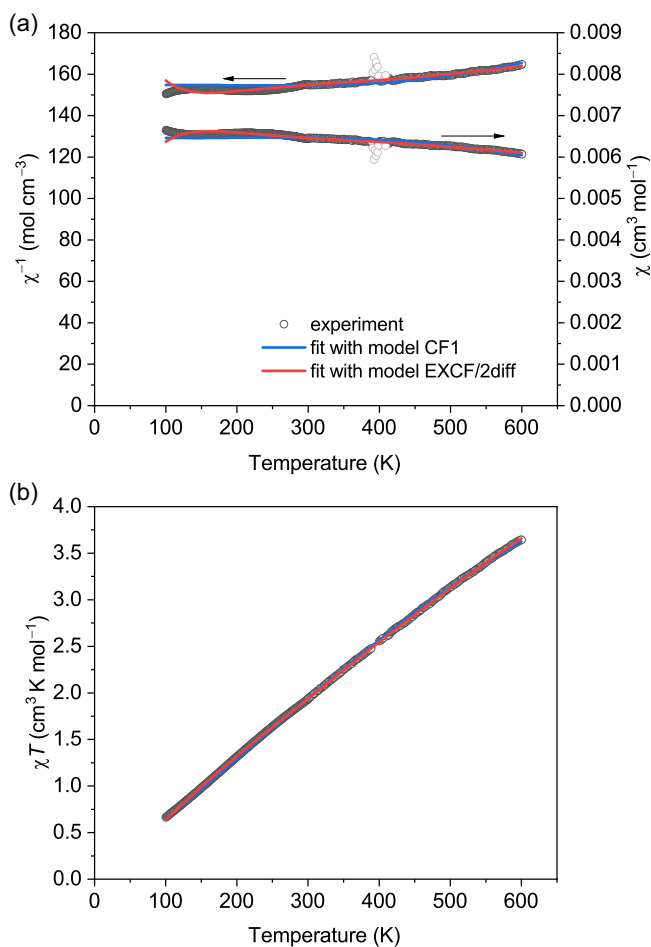


Figure 4. a) χ^{-1} and b) χT versus temperature T plots from 100 to 600 K that were obtained experimentally for $\text{Co}_2\text{Si}_5\text{N}_8$ (open circles) by combining the low-temperature with the HT susceptibility measurements together with fits (solid lines) according to the magnetic models CF/1 and EXCF/2diff.

susceptibility χ of $\text{Co}_2\text{Si}_5\text{N}_8$ is quasi-constant and only decreases by $-8.7(1)\%$ from $6.65 \times 10^{-3} \text{ cm}^3 \text{ mol}^{-1}$ at 100 K to $6.07 \times 10^{-3} \text{ cm}^3 \text{ mol}^{-1}$ at 600 K. For comparison, if the two Co ions in $\text{Co}_2\text{Si}_5\text{N}_8$ would be represented by two free localized and noninteracting spin $S = 3/2$ (Langevin paramagnetism), the spin-only susceptibility would follow the Curie law $\chi_c = C_c/T$, with the Curie constant $C_c = 3.75 \text{ cm}^3 \text{ K mol}^{-1}$. In this case, the susceptibility would drop strongly by -500% from $37.5 \times 10^{-3} \text{ cm}^3 \text{ mol}^{-1}$ at 100 K to $6.25 \times 10^{-3} \text{ cm}^3 \text{ mol}^{-1}$ at 600 K. The quasi-temperature-independent susceptibility found for $\text{Co}_2\text{Si}_5\text{N}_8$ also finds its expression in the characteristic χT evolution (Figure 4b) with an approximate linear increase of the susceptibility with temperature. In contrast, for a hypothetical Langevin paramagnet $\chi T = C_c/T \cdot T = C_c$ would be constant over temperature. As the susceptibility χ is approximately constant over temperature for $\text{Co}_2\text{Si}_5\text{N}_8$, also the inverse susceptibility χ^{-1} is approximately constant over temperature (Figure 4a). Again, this is in strong contrast to what would be found for a conventional Langevin paramagnet where $\chi^{-1} = C_c^{-1}T$ would increase linearly with the temperature.

In the following, a phenomenological Hamiltonian approach is used to refine quantum mechanical (QM) magnetic models to the experimentally observed susceptibility versus temperature datasets of $\text{Co}_2\text{Si}_5\text{N}_8$. Two different QM models will be introduced in order to get more insight why $\text{Co}_2\text{Si}_5\text{N}_8$ shows a quasi-temperature-independent paramagnetic susceptibility over such a broad temperature range.

2.2.2. Magnetic Model Refinement to TIP Susceptibility Data

The phenomenological Hamiltonian $\hat{H} = \hat{H}_{\text{SO}} + \hat{H}_{\text{EX}} + \hat{H}_{\text{CF}} + \hat{H}_{\text{ZEE}}$ takes into account the SO coupling, the exchange coupling (EX), the crystal-field (CF) interactions, and the ZEE effect to describe the energy within the framework of an angular momentum basis set (see Equation (S1), Supporting Information, for description of individual definitions of the Hamiltonian terms). Each site i of the magnetic model is characterized by its total atomic orbital angular momentum L_i and its total spin angular momentum S_i that span the basis states of the system $|L_i, m_{L_i}, S_i, m_{S_i}\rangle$, with the magnetic quantum number m_{L_i} and the magnetspin quantum number m_{S_i} . It should be noted that for the models applied in this work the SO coupling has not explicitly been applied, but is still included in the aforementioned Hamiltonian for completeness.

The simplest QM single-site model to simulate a TIP for a polycrystalline sample can be constructed from a $J = S = 1$ state (with “effective” spin S and total angular momentum J), with the eigenvalues in the z -basis being $|1, +1\rangle_z = (1, 0, 0)$, $|1, 0\rangle_z = (0, 1, 0)$, and $|1, -1\rangle_z = (0, 0, 1)$. When such a $J = 1$ state is exposed to a comparably strong uniaxial positive CF of 1000 cm^{-1} in z -direction, parameterized by the CF parameter (CFP) B_2^0 , the excited degenerated doublet states $|1, +1\rangle_z$ at energy E_2^z and $|1, -1\rangle_z$ at energy E_1^z are located 3000 cm^{-1} above the GS $|1, 0\rangle_z$ at energy E_0^z in zero magnetic field. If an external magnetic field H_z is applied in the z -direction, the doublet’s energy levels are split according to the ZEE diagram shown in Figure 5a. At an arbitrarily chosen magnetic field of $H_z = 5 \text{ kOe}$ (typical order of magnitude for a susceptibility measurement), the single-crystal susceptibility χ_z along the z -direction remains small and increases only slightly from quasi-zero to only $1.68688 \times 10^{-5} \text{ cm}^3 \text{ mol}^{-1}$ from 0 to 800 K, respectively. This is due to the very strong uniaxial CF that causes the nonmagnetic $|1, 0\rangle_z$ state to be the GS (see dashed lines in Figure 5c). On the other side, an external magnetic field $H_{x,y}$, either applied along the x - or the y -direction, i.e., perpendicular to the uniaxial CF, has a totally different effect, as illustrated in Figure 5b. Before the effect of this transverse external field is considered, it is convenient to transform the three eigenstates to a more appropriate set of states: whereas the GS remains $|1, 0\rangle_z$, the first excited state transforms from $|1, -1\rangle_z$ to $|1, 0\rangle_x$ and the second excited state from $|1, 1\rangle_z$ to $|1, 0\rangle_y$.

The considerations here will be restricted for a field applied in x -direction, but the y -direction case can be treated in an analogue way. With increasing H_x field, more and more of the $|1, -1\rangle_x$ state (“magnetic along x -direction”) is mixed to the (nonmagnetic) GS $|1, 0\rangle_z$ to form a new state with E_0^x . As shown in Figure 5d, the amount of the $|1, -1\rangle_x$ state that is mixed to the $|1, 0\rangle_z$ state is very small, i.e., only about 0.4% at a field of

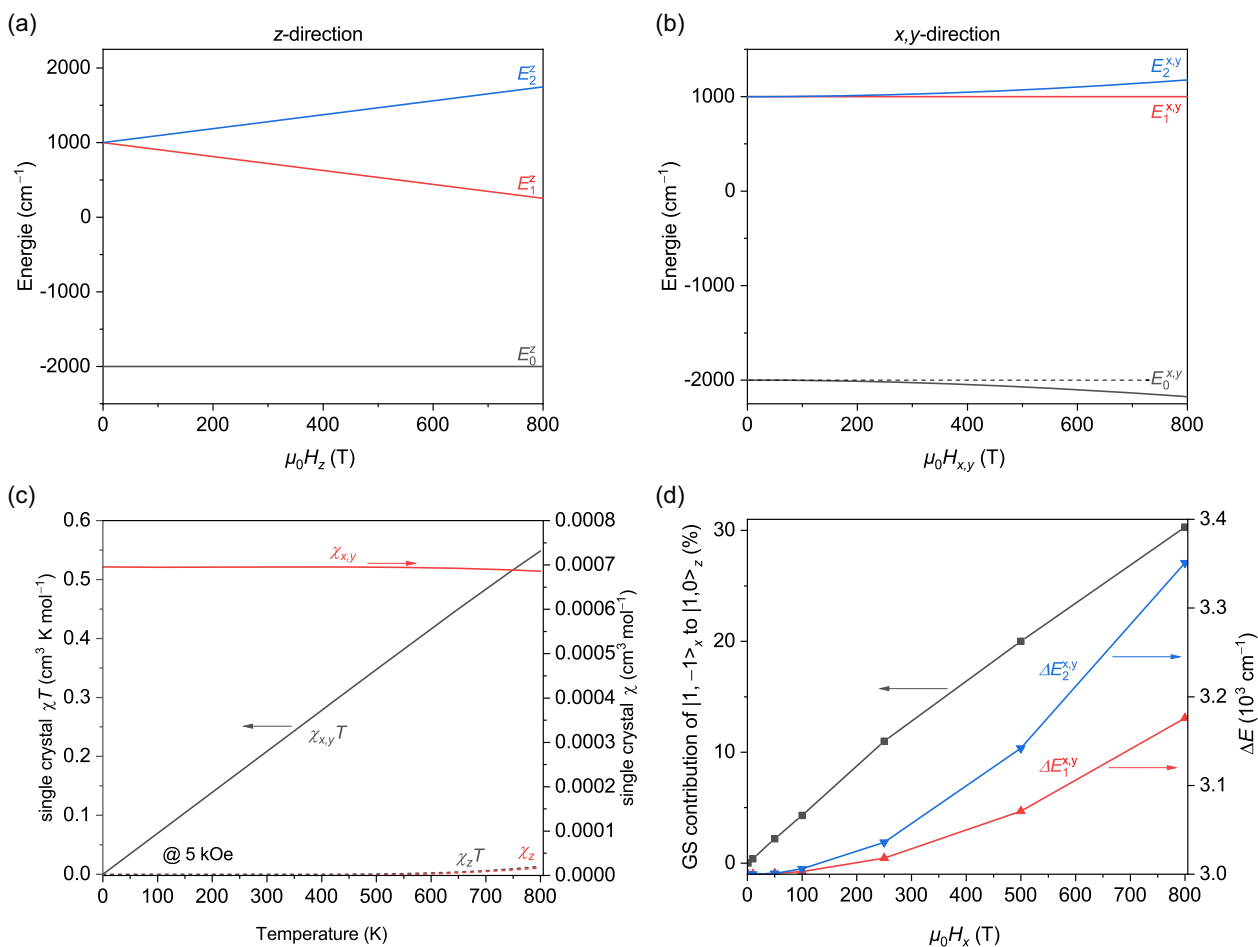


Figure 5. Calculations for model CF/1: a) ZEE diagram with applied magnetic field along z-direction, b) ZEE diagram with applied field along x- or y-direction, c) temperature dependence of molar susceptibility for magnetic field either applied in z- or in x/y-direction, and d) contribution of the $|1, -1\rangle_x$ state to the $|1, 0\rangle_z$ GS in dependence of the magnetic field applied along the x-direction.

$\mu_0 H = 10$ T. Also, the corresponding changes of energies $\Delta E_2^x = E_2^x - E_0^x$ and $\Delta E_1^x = E_1^x - E_0^x$ (same holds when x is substituted by y) are negligibly small for fields up to 10 T and only become significant for much higher fields. The lowering of the GS's energy is partially compensated by a simultaneous increase of energy of the excited $|1, 0\rangle_y$ state that is mixed with the $|1, 1\rangle_x$ state by H_x to form the highest state with energy E_2^x . The magnetic field along the x -direction does not affect the energy E_1^x of the $|1, 0\rangle_x$ state that is nonmagnetic in this direction. The mixing of the $|1, -1\rangle_x$ state with the nonmagnetic GS $|1, 0\rangle_z$ by a magnetic field in x -direction (in analogy the same holds for the y -direction) results in a temperature-independent paramagnetic susceptibility χ_x (solid red line in Figure 5c) that is realized over a wide temperature region from zero to 800 K with $\approx 7 \times 10^{-4}$ cm³ mol⁻¹. The quasi-constant χ_x causes $\chi_x T$ (solid black line in Figure 5c) to increase linearly with temperature. As χ_x and χ_y are quantitatively strongly dominating over the contributions from χ_z , the susceptibility of a polycrystalline sample mainly reproduces $\chi_{x,y}$. It is an important result so far that the uniaxial positive CF (B_0^z), referred to the z -basis, together with the possibility to apply magnetic fields along all principal axis,

as realized for a susceptibility measurement of a polycrystalline sample for instance, is capable to reproduce a TIP behavior over a broad temperature range.

In order to reproduce the quasi-temperature-independent paramagnetic susceptibility as experimentally observed for Co₂Si₅N₈, the so far presented simple model with only a single $J = 1$ magnetic center is slightly extended to a magnetic model called CF/1 by introducing a refinable effective g -factor g_{eff} that offers scaling abilities to the created effective paramagnetic moment stemming from the $J = 1$ effective angular momentum and by allowing the CFP B_0^z to be refined (see also Table 1). As presented in Figure 4, the experimental susceptibility curves from 100 to 600 K can well be simulated with a refined $g_{\text{eff}} = 4.86(1)$ and a CFP of $B_0^z = 414(2)$ cm⁻¹. The ZEE diagram of model CF/1 for the polycrystalline case is shown in Figure 6a.

The simplicity of model CF/1 allows to get some illustrative insight in how an uniaxial CF (parameterized by $B_0^z > 0$) can lead to a TIP behavior in a polycrystalline sample due to magnetic fields perpendicular to the z -axis. The TIP, as realized according to model CF/1, can be understood as “real” TIP because it consists of a GS with a small field-induced magnetic moment

Table 1. Refined parameters of magnetic models CF/1 and EXCF/2diff to experimental susceptibility versus temperature data for $\text{Co}_2\text{Si}_5\text{N}_8$, with total “effective” angular momentum quantum number J (fixed to $3/2$), effective isotropic g -factor g_{eff} , CFP B_0^2 , and isotropic magnetic exchange parameter J_{iso} between magnetic site 1 and 2.

Magnetic site	Parameter	EXCF/2diff	CF/1
1	J	$3/2$	1
	g_{eff}	3.82(1)	4.86(1)
	B_0^2 [cm^{-1}]	119(2)	414(2)
2	J	$3/2$	–
	g_{eff}	2.273(6)	–
	B_0^2 [cm^{-1}]	–	–
$1 \leftrightarrow 2$	J_{iso} [cm^{-1}]	–141(1)	–

without any other thermally accessible excited state present that could contribute with a magnetic moment. However, model CF/1 does not take into account at all the given real situation in $\text{Co}_2\text{Si}_5\text{N}_8$ regarding the two different Co sites with individual ligand coordinations, spin and orbital momenta, nor does it consider any interactions between the two sites. It is an important result, though, that even CF/1 is capable to model the experimental data adequately because any other, more complex magnetic model might suffer from overparametrization.

Model EXCF/2diff more adequately describes the actual situation of $\text{Co}_2\text{Si}_5\text{N}_8$ by introducing two different Co1 and Co2 species with individual local atomic coordinations. It is reasonable to assume that the Co ions that substitute the Ca^{2+} are also present as Co^{2+} in $\text{Co}_2\text{Si}_5\text{N}_8$ and preliminary X-ray absorption spectroscopy measurements support this assumption. Co^{2+} , as free ion, possesses an $[\text{Ar}]3d^7$ electronic configuration with a sevenfold degenerated 4F ground term and a 4P as first excited term, for instance. A hypothetical octahedral coordination would split the d orbitals into three t_{2g} and two e_g single-electron orbitals, respectively, separated by the CF splitting energy. In the d^7 many electron picture, the 4F ground term would split into a 4T_1 ground, a first excited 4T_2 and a second excited 4A_2 term (high-spin scenario). The threefold degenerate 4T_1 ground term allows in principle orbital momentum contribution (not quenched) to the total angular momentum. On the other side, an ideal tetrahedral coordination exhibits two e and three t_2 single-electron orbitals at lower and higher energy, respectively. Here, the 4F ground term splits into a 4A_2 ground, a first excited 4T_2 and a second excited 4T_1 state, i.e., the orbital momentum would be quenched. A square pyramidal coordination results in similar single-electron orbitals as the octahedral coordination, but the low-lying t_{2g} splits into a nondegenerated b_2 at lowest energy and a twofold degenerated e at somewhat higher energy. Further, the twofold degenerated e_g from the octahedral coordination splits into a lower a_1 and a somewhat higher b_1 single-electron orbital. An important fact is that a multiplicity of $4 = 2S + 1$, i.e., $S = 3/2$, is realized in a high-spin scenario with a corresponding spin-only magnetic moment of $\mu_{\text{SO}} = 2\sqrt{S(S+1)} \mu_{\text{B}} = 3.87 \mu_{\text{B}}$ for any of these coordinations. The coordination mainly determines whether a contribution

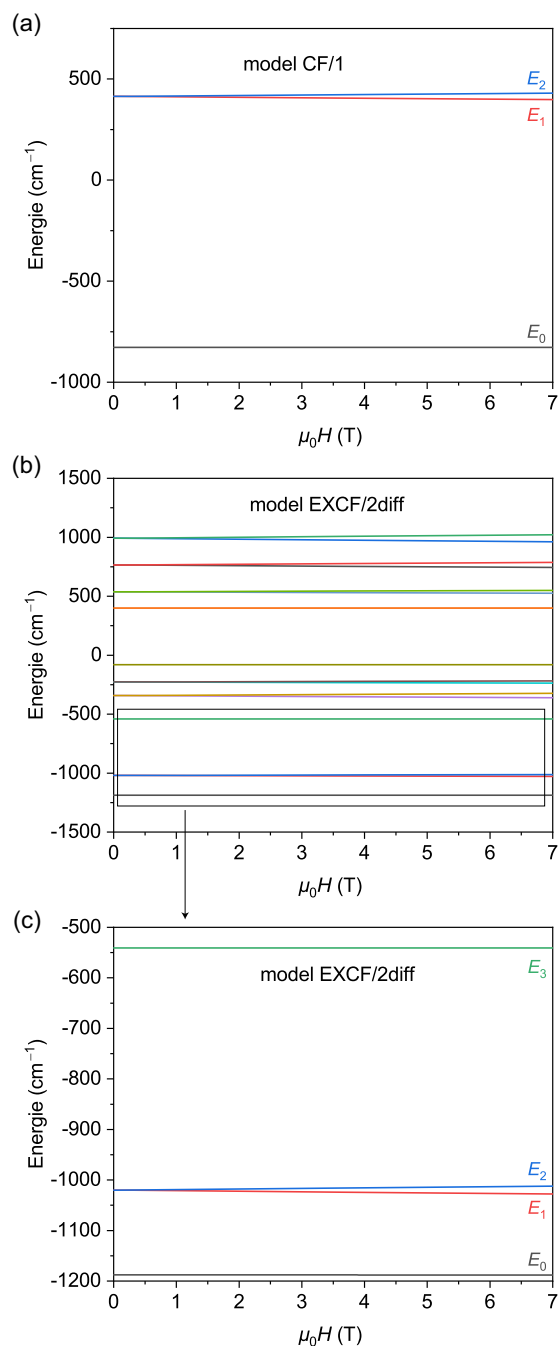


Figure 6. Calculated ZEE diagrams (polycrystalline sample case) according to the refined parameters obtained by a fit of magnetic model a) CF/1 and b) EXCF/2diff to the experimental susceptibility data of $\text{Co}_2\text{Si}_5\text{N}_8$. The parameters used for the calculations are listed in Table 1. c) shows an enlarged section of what is shown in (b).

from orbital momentum is present or not. In $\text{Co}_2\text{Si}_5\text{N}_8$, Co1 and Co2 occupy two different crystallographic sites that offer a (distorted) squared pyramidal N-coordination for the first and a distorted tetrahedral N-coordination for the latter Co species (see Figure S2, Supporting Information). In the considerations above, the high symmetric quadratic pyramidal as well as the

tetrahedral coordination would quench the orbital momentum and no local crystalline anisotropy would be present. However, the SO coupling, which did not play a role in the purely symmetric consideration above, principally can cause a “reinstallation” (second-order perturbation by the SO coupling) of some orbital momentum that then also results in crystalline anisotropy and in a distortion of the ideal coordination polyhedra. Also, given distortions of the coordination polyhedra that are not induced by the SO coupling allow in principle for a partial contribution of orbital momentum and for single-site anisotropy.

Following the considerations above, the model EXCF/2diff is composed of two magnetic sites, each with an “effective” total angular momentum quantum number $J = 3/2$. That means that J is set equal to the spin quantum number $S = 3/2$ that can be ascribed to a Co^{2+} with three unpaired electrons. Each of these sites possesses a refinable effective g -factor g_{eff} to account for eventual orbital momentum contributions to the effective paramagnetic moment. Only the first magnetic center is further exposed to an uniaxial CF that is parameterized by the CFP B_0^2 . Magnetic center 1 is connected to center 2 by introducing isotropic magnetic exchange interaction, parameterized by the exchange constant J_{iso} . As shown in Figure 4, this model is also capable to adequately describe the quasi-temperature-independent susceptibility over the broad temperature range from 100 to 600 K. The refined parameters of this model that reproduces the experimental observations with smallest residuals are summarized in Table 1. For site 1, a significant uniaxial CFP of $B_0^2 = 119(2) \text{ cm}^{-1}$ has been refined. The fact that $B_0^2 > 0$ means for a $J = 3/2$ that the Kramer-pair $m_j = \pm 3/2$ is higher in energy than the $m_j = \pm 1/2$ pair. Further, for site 1 a considerably larger $g_{\text{eff}} = 3.82(1)$ has been refined than for site 2 with $g_{\text{eff}} = 2.273(6)$. Site 1 and site 2 interact with each other via an isotropic antiferromagnetic exchange with $J_{\text{iso}} = -141(1) \text{ cm}^{-1}$. The refined parameters for model EXCF/2diff can be interpreted as having site 1 with a significant contribution of orbital momentum (larger g_{eff}) and, as a consequence, also uniaxial anisotropy (B_0^2). This would be in agreement with a Co^{2+} in a distorted tetrahedral coordination. For site 2, it is indicated that the magnetic moment essentially stems from the spin without significant contribution from orbital momentum (g_{eff} close to 2). This would be in agreement with a Co^{2+} in square pyramidal coordination and quenched orbital momentum. However, it should be taken into account that site 1 and site 2 form a QM system together due to the antiferromagnetic interaction and the CF formally acting only on site 1 plays a role for the whole system, i.e., for both sites. Figure 6b shows the ZEE diagram (with z magnetic field axis) of model EXCF/2diff for the polycrystalline case. Most important for the magnetic properties are the low-lying states and their energy dependence on the magnetic field. The simple model CF/1 can cause a “real” TIP behavior by exhibiting a magnetic GS without any other thermally accessible excited magnetic state when no magnetic field is applied. The first excited magnetic doublet state is located $3|B_0^2| \approx 1242 \text{ cm}^{-1}$ (corresponds to a thermal energy of about 1787 K) above the nonmagnetic GS. However, magnetic fields within the easy x - y -plane create a GS that exhibits a small magnetic moment by QM mixing higher magnetic states into the ground state. This magnetic GS without any other thermally accessible magnetic state leads to “real” TIP behavior here.

The situation is different for the model EXCF/2diff: At zero magnetic field, there exists a “nonmagnetic” singlet GS but with an excited “magnetic” doublet state only $\approx 168 \text{ cm}^{-1}$ higher in energy (corresponds to a thermal energy of about 242 K), which is accessible by thermal population in the investigated temperature regime. Therefore, according to the ZEE energy levels with thermal accessible magnetic states, model EXCF/2diff cannot cause a pure and “real” TIP behavior (see also below). Still, the more complex model EXCF/2diff with two $J = 3/2$ centers that interact via an isotropic (antiferromagnetic) exchange and where at least one center is exposed to an uniaxial CF is again capable to model the quasi-temperature-independent susceptibility, at least in the specified temperature region from 100 to 600 K.

In a simplified picture, the two $J = 3/2$ centers (16-fold degeneracy) form a singlet, a triplet, a quintet, and a septet state due to antiferromagnetic coupling, each separated in energy at zero magnetic field. For the magnetic properties, only the low-lying singlet and triplet terms play a role and need to be considered further. The nonmagnetic singlet GS with an “effective” total angular momentum of the complete spin system $J_s = 0$ results from the antiferromagnetic interaction of the two spins. This singlet is actually composed out of four basis states $(-\frac{1}{2}|+\frac{1}{2}\rangle, (+\frac{1}{2}|-\frac{1}{2}\rangle, (-\frac{3}{2}|+\frac{3}{2}\rangle, \text{ and } (+\frac{3}{2}|-\frac{3}{2}\rangle)$ in $(m_j(1)|m_j(2))$ notation. The triplet with effective total angular momentum $J_s = 1$ represents the first excited state that exhibits a permanent magnetic moment. With the singlet GS remaining unaffected, the action of the CF finally causes the first excited triplet state to split into a lower energy $m_j = \pm 1$ doublet state and a $m_j = 0$ singlet state at higher energy, with the latter having little effect on the magnetic properties. Essentially, the three lowest lying states of the model EXCF/2diff are a nonmagnetic singlet as GS and a magnetic doublet as first excited state at zero-field that can significantly be occupied within the typical temperature regime of the experiment (see Figure 6c). Mixing of “magnetic states” into a formerly nonmagnetic GS by magnetic fields within the easy x - y -plane of the single-ion anisotropy, as identified to play a crucial role for model CF/1, might also play an additional role for the magnetic properties realized by the more complex model EXCF/2diff. However, the interplay of the antiferromagnetic exchange interaction between the two Co centers together with the single-ion anisotropy (at least present for one of the two Co sites) that constitutes model EXCF/2diff is supposed to play the crucial role for $\text{Co}_2\text{Si}_5\text{N}_8$. That means that the observed TIP is not caused by a field-induced “magnetic” GS, but by a delicate quantitative interplay of exchange interaction and single-ion anisotropy, both with a characteristic, but principally different temperature dependency. The interplay and mutual compensation finally leads to the observed realization of a quasi-TIP over a certain temperature range that is, referring also to ref. [38], classified here as a pseudo-TIP.

Overall, the magnetic properties found for polycrystalline $\text{Co}_2\text{Si}_5\text{N}_8$ are very similar to those reported for the dinuclear Co^{2+} complex $[\text{Co}_2\text{PdCl}_2(\text{dpa})_4]^{[36]}$ with quasi-temperature-independent paramagnetic susceptibilities of $6.5 \times 10^{-3} \text{ cm}^3 \text{ mol}^{-1}$ ($\text{Co}_2\text{Si}_5\text{N}_8$) and $10 \times 10^{-3} \text{ cm}^3 \text{ mol}^{-1}$ ($\text{Co}_2\text{PdCl}_2(\text{dpa})_4$) over a broad temperature range (above 100 K). The Co ion distribution in $\text{Co}_2\text{Si}_5\text{N}_8$ is characterized by a 1D chain arrangement with additional slight

dimerization (see Figure 2c). Two edge sharing Co–N–polyhedra form the base unit according to this dimerization with resulting Co1–N–Co₂ coupling paths. These Co-dimer units exhibit a high degree of similarity to the Co–Pd–Co coupling paths of the [Co₂PdCl₂(dpa)₄] complex.^[36] The antiferromagnetic coupling between the Co ions within these dimers together with single-ion anisotropy is therefore supposed to represent prerequisites for the realization of the pseudo-TIP behavior, for the complex as well as for the crystalline nitridosilicate Co₂Si₅N₈.

2.2.3. Low-Temperature Magnetic Properties

Returning to the low-temperature magnetic properties, the zero-field cooled (ZFC)/field cooled (FC) susceptibility versus temperature plots (see Figure 3b) for pristine Co₂Si₅N₈ show a bifurcation of the ZFC and FC branch below ≈10 K (at 0.25 kOe magnetic field). The higher the magnetic field of measurement, the lower the temperature of ZFC/FC bifurcation, as it is characteristic for a ferrimagnetic order with antiferromagnetic sublattice coupling. The low value of magnetization of only 0.094(1) μ_B per Co ion at 70 kOe and 2 K further reveals that this magnetic order cannot be ascribed to a pure ferromagnetic order of the Co ions of the Co₂Si₅N₈ main phase, for instance, that would contribute at least with about 1 μ_B per Co ion for hypothetical saturation. The irreversible processes found below ≈10 K that are most probably connected to ferri-/ferromagnetic domain formations (magnetic hysteresis) need either be ascribed to a ferrimagnetic ordering of the Co₂Si₅N₈ main phase at very low temperature or to the presence of small amounts of a ferri-/ferromagnetic impurity phase. In the following, it will be outlined why the presence of an additional nano crystalline ferrimagnetic phase seems more plausible than a ferrimagnetic ordering of the main phase. A deviation from the TIP behavior in form of a steep increase of the susceptibility at low temperature of ≈100 K was also observed for the [Co₂PdCl₂(dpa)₄] complex^[36] and ascribed to an impurity phase in the sample.

In agreement with the bifurcation of the ZFC/FC branch below ≈10 K, the full loop magnetic field scans (Figure 3c,d) exhibit remanent magnetizations (10⁻³ μ_B per Co)/coercivity fields (Oe) of 9.2(1)/760(10), 1.9(1)/140(10), 0.5(1)/40(10), and 0.1(1)/0(10) at 2, 5, 7.5, and 10 K, respectively. Very similar ferrimagnetic properties with the bifurcation of the ZFC/FC branch below ≈10 K and a coercivity field of 300 Oe at 5 K have been reported by Yin et al.^[45] for nanocrystalline Co₃O₄. If only about 5 at% of all Co ions within the measured Co₂Si₅N₈ sample would contribute to such a nanocrystalline Co₃O₄ phase, they would reproduce the observed remanent magnetization value at 5 K. As the ferrimagnetic properties of the nanocrystalline Co₃O₄ phase strongly depend on the real structure and on surface defects, such quantitative estimations remain unavoidably vague. As outlined in detail in the Supporting Information, 5 wt% of a Co₃O₄ phase with a small crystallite size of only 5 nm and correspondingly broadened reflections cannot be detected in the XRD pattern when present besides the Co₂Si₅N₈ main phase (see Figure S5, Supporting Information). In agreement with the observation of ZFC/FC bifurcation at about 10 K, the maximum slope of χ' and the onset of χ'' of the alternating current (AC) susceptibility measurement (Figure 7a) are also located at

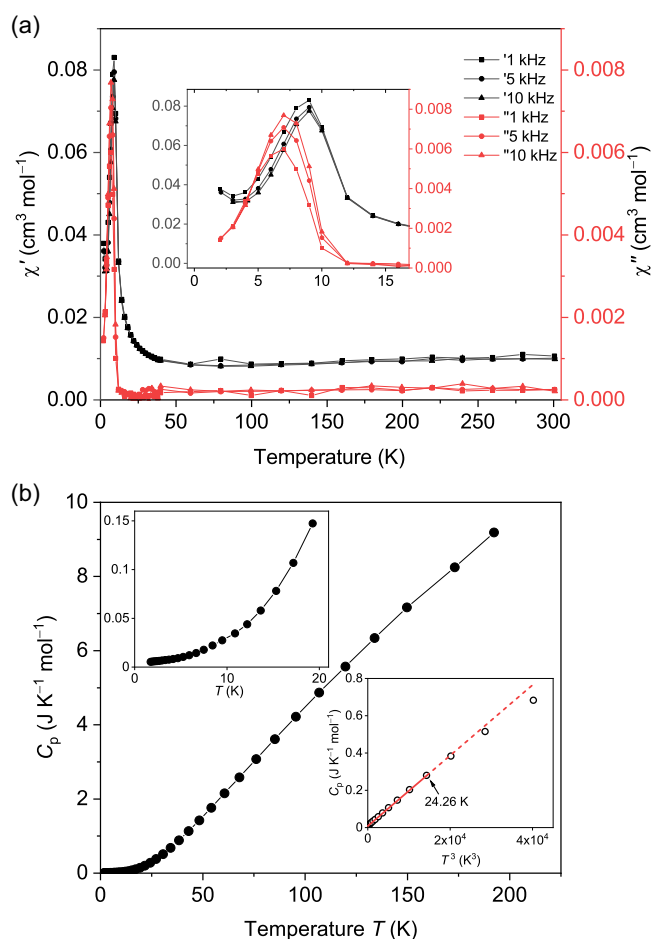


Figure 7. a) Real χ' and imaginary χ'' part of AC susceptibility measured for Co₂Si₅N₈ in zero DC field for 1, 5, and 10 kHz excitation frequency. Error bars are smaller than symbols. b) Isobaric heat capacity C_p measured for pristine Co₂Si₅N₈ in zero DC field. The upper left inset shows a magnified section of the heat capacity in the low-temperature region and the lower right inset presents a plot of C_p versus T³ in the low-temperature region together with a linear fit (solid line) and its extrapolation (dashed line). Error bars are smaller than symbols.

10 K, confirming thereby a magnetic phase transition from paramagnetic to ferri-/ferromagnetic to occur at this temperature.^[46]

In contrast, the heat capacity C_p versus temperature curve (Figure 7b) does not give any indication for a phase transition to occur at around 10 K (see left inset in Figure 7b). From 1.8 to 24.26 K, well below the Debye temperature T_D, the heat capacity follows the characteristic C_p = αT³ = (12π⁴N_Ak_B)/(5T_D³) · T³ law^[47,48] (with N_A and k_B as Avogadro and Boltzmann constant, respectively) that is realized if only lattice vibrations contribute to the heat capacity (see right inset in Figure 7b). The Debye temperature T_D has been refined to 468(2) K, a relatively high value, that is, however, in agreement with the fact that even at 292(1) K the measured heat capacity is only 13.60(4) JK⁻¹mol⁻¹ and still well below the Dulong–Petit limit of ≈24.94 JK⁻¹mol⁻¹. The high Debye temperature of Co₂Si₅N₈ can be explained by the very stiff SiN₄ units in which internal vibrational modes contribute to the heat capacity only at

comparably HTs. The fact that the heat capacity below ≈ 25 K can solely be explained by lattice vibration contributions further supports the claim that the main phase does not exhibit a paramagnetic to ferrimagnetic phase transition, but that some minor amounts of an additional phase, as the above mentioned nano crystalline Co_3O_4 , are present here. Very small amounts of such an additional nanocrystalline Co_3O_4 impurity would still be capable to cause the corresponding features observed in the DC and AC magnetometry measurements, but would not contribute noticeably to the heat capacity signal. In conclusion, the $\text{Co}_2\text{Si}_5\text{N}_8$ main phase exhibits a pseudo-TIP from about 600 to 100 K. On the other side, at temperatures below ≈ 10 K, the ferrimagnetic ordering of an additional nano crystalline Co_3O_4 impurity phase is indicated by the combined results from all applied methods.

The question about what causes the susceptibility to increase in the intermediate temperature region from about 100–10 K will be addressed in the following: By a modified Curie–Weiss law according to $\chi_{\text{CW}} = C/(T - T_{\text{CW}}) + \text{TIP}$, with the Weiss constant T_{CW} , the experimental susceptibility data from 15 (above the ferrimagnetic transition) to 390 K can be described with moderate agreement between fit curve and experimental dataset (see Figure S6, Supporting Information). The modified Curie–Weiss fit returns the expected (pseudo) TIP susceptibility of $6.02(1) \times 10^{-3} \text{ cm}^3 \text{ mol}^{-1}$, a Weiss constant of $T_{\text{CW}} = 9.51(2)$ K and a paramagnetic effective moment of $0.84(2) \mu_{\text{B}} \text{ f.u.}^{-1}$ $\text{Co}_2\text{Si}_5\text{N}_8$ that has been calculated from the Curie constant C . Roughly estimated, if the determined Curie constant C would instead exclusively be ascribed to 5 wt% of a Co_3O_4 phase, then each Co of that impurity phase would exhibit an effective paramagnetic moment of about $2.6(1) \mu_{\text{B}}$, what represents a reasonable value. From this side, it seems plausible that the increasing susceptibility from about 100 down to about 10 K is caused by the paramagnetic signal of the additional nano crystalline Co_3O_4 impurity phase above its ferrimagnetic ordering temperature. However, as already outlined above, between ≈ 100 and 10 K, a partial deviation of the magnetization versus magnetic field plots from a pure linear behavior (see Figure S3, Supporting Information) can also be attested. As a consequence, the increasing susceptibility values from about 100 down to about 10 K might at least partially also be caused by ferrimagnetic short-range ordering from the nanocrystalline Co_3O_4 impurity phase. As its ferrimagnetic properties strongly depend on real structure and density of surface defects that might vary over the sample, the ferrimagnetic transition could be “smeared out in temperature” instead of occurring sharply at around 10 K and thereby also affect the susceptibility between 100 and 10 K. As the temperature-independent susceptibility for $\text{Co}_2\text{Si}_5\text{N}_8$ is classified as pseudo-TIP, the increase of susceptibility from ≈ 100 to 10 K could at least partially also be caused by the $\text{Co}_2\text{Si}_5\text{N}_8$ main phase that simply does not exhibit pseudo-TIP behavior any more below about 100 K. The low-dimensional character of the Co^{2+} magnetic moments bearing chains in $\text{Co}_2\text{Si}_5\text{N}_8$ might suppress a 3D magnetic phase transition to an antiferromagnetic ordered state down to very low temperatures. Respectively, such an antiferromagnetic transition of the main phase below about 15 K might then be masked by the strong ferrimagnetic signal from the ferrimagnetic impurity phase.

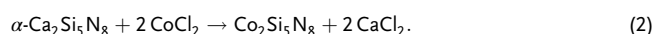
The magnetic properties found for $\text{Co}_2\text{Si}_5\text{N}_8$ are very different from those as reported for $\text{Fe}_2\text{Si}_5\text{N}_8$.^[23] By applying Mössbauer spectroscopy, high-spin states for Fe^{2+} were confirmed for $\text{Fe}_2\text{Si}_5\text{N}_8$ as expected from CF theory for the distorted tetrahedral environments. According to magnetic susceptibility measurements, $\text{Fe}_2\text{Si}_5\text{N}_8$ was claimed to exhibit paramagnetism with an effective paramagnetic moment of $\mu_{\text{eff}} = 3.2(1) \mu_{\text{B}}$ at 300 K that is strongly decreasing to about $0.4 \mu_{\text{B}}$ at lowest temperature of ≈ 5 K.^[23] An anomaly in the susceptibility curve at $T_{\text{N}} = 36.1$ K was ascribed to a ferro-/ferrimagnetic $\text{Fe}_{2-x}\text{Ca}_x\text{Si}_2\text{O}_6$ impurity phase. A TIP has not been reported for $\text{Fe}_2\text{Si}_5\text{N}_8$.

3. Conclusion

In this article, we reported a novel nitridosilicate $\text{Co}_2\text{Si}_5\text{N}_8$ and its magnetic properties. A thorough comparison of the crystal structure of $\text{Co}_2\text{Si}_5\text{N}_8$ with other related nitridosilicates $\text{M}_2\text{Si}_5\text{N}_8$ ($\text{M} = \text{Ca}, \text{Fe}$) was made. Here, it becomes visible that the cation size significantly influences the nitridosilicate structure and with it the size of the migration channels. Crystalline $\text{Co}_2\text{Si}_5\text{N}_8$ nitridosilicate exhibits two different Co sites with four- and fivefold N-coordination, respectively. These Co–N coordination polyhedra form edge-sharing quasi-1D chains with slightly dimerized Co1–N–Co2 magnetic exchange paths. A rather weak antiferromagnetic exchange interaction between these two Co species of such a dimer unit together with local anisotropy, that is at least realized for one Co site, finally causes a pseudo-TIP with a comparably high susceptibility of about $6.5 \times 10^{-3} \text{ cm}^3 \text{ mol}^{-1}$, observable from 100 to 600 K. With reference to Gendron and Autschbach,^[38] a pseudo-TIP results from a near-perfect cancellation of temperature-dependent contributions to the susceptibility that depends delicately on the mixing of ion levels in the electronic states, their relative energies, and the magnetic coupling between them. The pseudo-TIP behavior as found for $\text{Co}_2\text{Si}_5\text{N}_8$ is very similar to what has been reported for a $[\text{Co}_2\text{PdCl}_2(\text{dpa})_4]$ complex^[36] that only contains a single Co–Pd–Co dimeric unit per molecule. This suggests that a dimeric antiferromagnetic coupling path together with the presence of single-ion anisotropy represents a kind of prerequisite for the realization of a pseudo-TIP behavior. From the viewpoint of the authors, it would be desirable that the distinction between whether a real or a pseudo-TIP is realized would gain more relevance in this field of research. Even though both types of TIP phenomenologically appear as a positive susceptibility that is independent of temperature, the underlying quantum physics are fundamentally different comparing a real with a pseudo-TIP.

4. Experimental Section

Synthesis of $\text{Co}_2\text{Si}_5\text{N}_8$: This ion exchange route for synthesizing nitridosilicates has been established and described in detail by Bielec et al.^[22–25] Accordingly, the nitridosilicate $\text{Co}_2\text{Si}_5\text{N}_8$ was synthesized via an ion exchange route from $\alpha\text{-Ca}_2\text{Si}_5\text{N}_8$ according to



The ion exchange took place at 900 °C in nitrogen atmosphere where $\alpha\text{-Ca}_2\text{Si}_5\text{N}_8$ (white powder) and CoCl_2 (blue powder) were thoroughly mixed in an agate mortar and then filled into a sealed quartz ampoule.

For the synthesis of α -Ca₂Si₅N₈, 1.86 mmol Ca (dendritic pieces, 99.99%, Aldrich) and 3.02 mmol silicon diimide^[49] were synthesized according to the literature.^[4] For the synthesis of Co₂Si₅N₈, 385 mg α -Ca₂Si₅N₈ and 1000 mg CoCl₂ were thoroughly mixed in an agate mortar, filled into a quartz ampoule, and then sealed. The ion exchange took place at 900 °C under nitrogen atmosphere (in 3 h to 900 °C, hold for 3 h and in 10 h to 500 °C). After the reaction the quartz ampoule was opened and a dark brownish Co₂Si₅N₈ powder has been obtained that was washed with water to remove the metal halides. The fact that the complete white educt of α -Ca₂Si₅N₈ has been transformed into the dark brownish product indicates the complete transformation to Co₂Si₅N₈.

XRD: XRD experiments on powder samples of Co₂Si₅N₈ were performed on a STOE STADI P powder diffractometer in Debye–Scherrer geometry with Ge(111)-monochromatized Mo K_{α1} radiation ($\lambda = 0.709026$ Å). The sample was enclosed in a glass capillary of 0.3 mm diameter.

SEM/EDX: SEM was performed on a Zeiss Merlin microscope and for EDX analysis a Quantax 400 system from Bruker was used at an acceleration voltage of 10 kV.

DC Magnetometry: Physical properties were determined by using a physical property measurement system DynaCool from Quantum Design. The DC magnetic moment was measured with a vibrating sample magnetometry (VSM) option. 15.6 mg of pristine Co₂Si₅N₈ was filled into a polypropylene (PP) sample capsule (QDS-4096-388, Quantum Design) and attached to a brass sample holder (QDS-P125A, Quantum design). ZFC and FC magnetic moment versus temperature curves were obtained during heating at magnetic fields of 5, 2.5, and 0.25 kOe, respectively. From 2 to 50 K, the temperature was set in “settle mode” and from 50 to 300 K in “sweep mode” with 2 K min⁻¹, each with a temperature step size of $\Delta T = 1$ K. A further magnetic moment versus temperature scan was measured in FC mode for an extended temperature range from 10 to 390 K at a magnetic field of 5 kOe in “sweep mode” with 2 K min⁻¹. The signal averaging time per measuring point was 10 s for all DC measurements. The molar susceptibility χ refers to one mole of formula units Co₂Si₅N₈. DC Magnetic moment versus magnetic field curves were measured at 390, 350, 300, 250, 200, 150, 100, 75, 50, 40, 30, 20, 10, and 2 K from 70 kOe to zero magnetic field (one quadrant), respectively. Full loop (four quadrants) DC magnetic moment versus magnetic field curves were measured at 300, 150, 50, 35, 25, 15, 10, 7.5, 5, and 2 K, each loop starting at 70 kOe, i.e., no initial (virgin) curves were measured. The signal averaging time per measuring point was 10 s and each point was measured twice. The magnetic moment raw data of the temperature as well as for the field scans were corrected for diamagnetic contributions of the PP sample holder (-7.71429×10^{-9} emu Oe⁻¹) and for the atomic closed shells (-4.69507×10^{-5} cm³ mol⁻¹) according to the incremental method.^[50]

HT DC Magnetometry: High temperature (HT) DC magnetometry measurements were performed by using the VSM oven option from Quantum Design. A 13.7 mg Co₂Si₅N₈ powder pellet that had previously been used for the heat capacity measurement (see below) was mounted onto the heater stick using single-part water-based alumina cement (Zircar ceramics) as adhesive. The magnetic moment was measured at a field of 5 kOe from 300 to 880 K with a heating rate of 10 K min⁻¹ and then from 880 back to 300 K with a cooling rate of 10 K min⁻¹. The corresponding time–temperature plot is presented in Figure S4, Supporting Information, revealing that the requested cooling rate could only be realized for the higher temperature region due to the nonactive cooling procedure. The signal averaging time was 10 s per measuring point. After the HT experiment, a full loop DC magnetic moment versus field scan was measured at 300 K starting with the maximum field of 70 kOe. During the sample mounting procedure, a small amount of sample (≈ 5 wt%) might have been lost. As a consequence, for the quantitative data evaluation of the HT DC susceptibility data up to 600 K, the value at 300 K has been calibrated to the corresponding value (corrected for diamagnetic contributions) as obtained from the low-temperature VSM measurements as outlined above. Refinements of magnetic models utilizing the susceptibility versus temperature datasets have been performed using the program PHI.^[51]

AC Magnetometry: AC susceptibility was measured using an ACMS-II option (Quantum Design) with the PP sample capsule remounted to a

plastic straw (Quantum Design) with polyimide tape. AC susceptibility was measured from 300 to 5 K in zero DC field and with an AC excitation field of 5 Oe for excitation frequencies of 1, 5, and 10 kHz, respectively. Each measuring point was obtained by the three-point AC measuring mode with an averaging time of 10 s and a threefold redundancy. No corrections have been applied to the AC susceptibility raw data.

Heat Capacity: Isobaric heat capacity Cp in zero magnetic field was measured with a heat capacity option (Quantum Design) using the relaxation method. 13.7 mg of pristine Co₂Si₅N₈ powder was pressed into a 4 mm diameter pellet by applying 1.5 tons (Maassen Spektroskopie press assembly). An addenda measurement from 200 to 1.8 K with Apiezon N grease (Apiezon) on the sample platform has been performed at 37 temperatures with logarithmic distribution. The heat capacity of the Co₂Si₅N₈ powder sample was measured from 192 to 1.8 K with a 2% relative temperature raise at 42 different temperatures with logarithmic distribution. The thermal sample coupling for the whole measuring series is 94(3)%. The specific molar heat capacity is related to the total number of atoms within the sample and not to the number of formula units (there are 15 atoms within a formula unit).

Supporting Information

Supporting Information is available from the Wiley Online Library or from the author.

Acknowledgements

The authors gratefully acknowledge Udo Geckle (IAM-ESS KIT Karlsruhe) for the EDX measurements.

Open Access funding enabled and organized by Projekt DEAL.

Conflict of Interest

The authors declare no conflict of interest.

Data Availability Statement

The data that support the findings of this study are available from the corresponding author upon reasonable request.

Keywords

nitridosilicates, pseudo temperature independent paramagnetism, second-order Zeeman effects, temperature-independent paramagnetism, Van Vleck

Received: October 19, 2023

Revised: February 2, 2024

Published online:

- [1] P. Ball, *Nature* **2001**, 409, 974.
- [2] P. Pust, P. J. Schmidt, W. Schnick, *Nat. Mater.* **2015**, 14, 454.
- [3] C. Braun, M. Seibald, S. L. Börger, O. Oeckler, T. D. Boyko, A. Moewes, G. Miehe, A. Tücks, W. Schnick, *Chemistry* **2010**, 16, 9646.
- [4] S. R. Römer, C. Braun, O. Oeckler, P. J. Schmidt, P. Kroll, W. Schnick, *Chem. Eur. J.* **2008**, 14, 7892.
- [5] C. Braun, *Doctoral Thesis*, Ludwig-Maximilians-Universität, München, **2010**.
- [6] C. Braun, S. L. Börger, T. D. Boyko, G. Miehe, H. Ehrenberg, P. Höhn, A. Moewes, W. Schnick, *J. Am. Chem. Soc.* **2011**, 133, 4307.

- [7] C. Braun, H. Ehrenberg, W. Schnick, *Eur. J. Inorg. Chem.* **2012**, 2012, 3923.
- [8] R. Mueller-Mach, G. Mueller, M. R. Krames, H. A. Höpfe, F. Stadler, W. Schnick, T. Jüstel, P. Schmidt, *Phys. Status Solidi A* **2005**, 202, 1727.
- [9] Y. Q. Li, G. de With, H. T. Hintzen, *J. Mater. Chem.* **2005**, 15, 4492.
- [10] X. Piao, K. I. Machida, T. Horikawa, H. Hanzawa, *Appl. Phys. Lett.* **2007**, 91, 041908.
- [11] R.-J. Xie, N. Hirotsuki, Y. Li, T. Takeda, *Materials* **2010**, 3, 3777.
- [12] R. Mueller-Mach, G. O. Mueller, M. R. Krames, O. B. Shchekin, P. J. Schmidt, H. Bechtel, C.-H. Chen, O. Steigelmann, *Phys. Status Solidi RRL* **2009**, 3, 215.
- [13] T. Jüstel, H. Nikol, C. Ronda, *Angew. Chem., Int. Ed.* **1998**, 37, 3084.
- [14] C. Ronda, *Luminescence: From Theory to Applications*, Wiley-VCH, Weinheim **2008**.
- [15] W. Schnick, *Phys. Status Solidi RRL* **2009**, 3, A113.
- [16] *Seventh Int. Conf. on Solid State Lighting* (Eds: P. Schmidt, A. Tuecks, J. Meyer, H. Bechtel, D. Wiechert, R. Mueller-Mach, G. Mueller, W. Schnick, I. T. Ferguson, N. Narendran, T. Taguchi), Vol. 6669, Optical Engineering + Applications, San Diego, CA, **2007**.
- [17] K. Uheda, S. Shimooka, M. Mikami, H. Imura, N. Kijima, in *Proc. of 14th Int. Display Workshops*, Society for Information Display, Sapporo, Japan, December **2007**, pp. 899–902.
- [18] S. Schmiechen, P. Pust, P. J. Schmidt, W. Schnick, *Nachr. Chem.* **2014**, 62, 847.
- [19] P. Pust, F. Hintze, C. Hecht, V. Weiler, A. Locher, D. Zitnanska, S. Harm, D. Wiechert, P. J. Schmidt, W. Schnick, *Chem. Mater.* **2014**, 26, 6113.
- [20] P. Pust, V. Weiler, C. Hecht, A. Tücks, A. S. Wochnik, A.-K. Henß, D. Wiechert, C. Scheu, P. J. Schmidt, W. Schnick, *Nat. Mater.* **2014**, 13, 891.
- [21] E. Elzer, P. Strobel, V. Weiler, M. R. Amin, P. J. Schmidt, A. Moewes, W. Schnick, *Chemistry* **2022**, 28, e202104121.
- [22] P. Bielec, W. Schnick, *Angew. Chem., Int. Ed.* **2017**, 56, 4810.
- [23] P. Bielec, O. Janka, T. Block, R. Pöttgen, W. Schnick, *Angew. Chem., Int. Ed.* **2018**, 57, 2409.
- [24] P. Bielec, R. Nelson, R. P. Stoffel, L. Eisenburger, D. Günther, A.-K. Henß, J. P. Wright, O. Oeckler, R. Dronskowski, W. Schnick, *Angew. Chem., Int. Ed.* **2019**, 58, 1432.
- [25] P. Bielec, *Doctoral Thesis*, Ludwig-Maximilians-Universität, München, **2018**.
- [26] H. Huppertz, N. Stock, W. Schnick, *Adv. Mater.* **1996**, 8, 844.
- [27] B. N. Figgis, J. Lewis, *The Magnetic Properties of Transition Metal Complexes*, Vol. 6, Progress in Inorganic Chemistry, Interscience Publishers, New York **1964**.
- [28] J. H. van Vleck, *Nobel Lecture*, Harvard University, Cambridge, MA, December **1977**.
- [29] J. H. van Vleck, *Phys. Rev.* **1928**, 31 587.
- [30] W. Nolting, A. Ramakanth, *Quantum Theory of Magnetism*, Scholars Portal, Berlin, Heidelberg **2009**.
- [31] J. M. Coey, *Magnetism and Magnetic Materials*, Cambridge Univ. Press, New York **2010**.
- [32] Y. Takikawa, S. Ebisu, S. Nagata, *J. Phys. Chem. Solids* **2010**, 71, 1592.
- [33] A. Carrington, *Mol. Phys.* **1960**, 3, 271.
- [34] B. N. Figgis, *Trans. Faraday Soc.* **1960**, 56, 1553.
- [35] R. Schlapp, W. G. Penney, *Phys. Rev.* **1932**, 42, 666.
- [36] W. van den Heuvel, L. F. Chibotaru, *Inorg. Chem.* **2009**, 48, 7557.
- [37] O. Kahn, *Molecular Magnetism*, Wiley-VCH, New York **2001**.
- [38] F. Gendron, J. Autschbach, *J. Phys. Chem. Lett.* **2017**, 8, 673.
- [39] J. Rodriguez-Carvajal, *Phys. B*, **1993**, 192, 55.
- [40] J. F. Béjar, P. Lelann, *J. Appl. Crystallogr.* **1991**, 24, 1.
- [41] T. Schlieper, W. Milius, W. Schnick, *Z. Anorg. Allg. Chem.* **1995**, 621, 1380.
- [42] T. Schlieper, W. Schnick, *Z. Anorg. Allg. Chem.* **1995**, 621, 1037.
- [43] The term dreier ring was coined by Liebau and is derived from the German word “drei”, which means three; however, a dreier ring is not a three-membered ring, but a six-membered ring comprising three tetrahedral centers (si) and three electronegative atoms.
- [44] M. Zeuner, S. Pagano, W. Schnick, *Angew. Chem., Int. Ed.* **2011**, 50, 7754.
- [45] K. Yin, J. Ji, Y. Shen, Y. Xiong, H. Bi, J. Sun, T. Xu, Z. Zhu, L. Sun, *J. Alloys Compd.* **2017**, 720, 345.
- [46] M. Balanda, *Acta Phys. Pol. A* **2013**, 124, 964.
- [47] G. Joos, *Lehrbuch Der Theoretischen Physik*, 14. ed., Akad. Verl.-Ges., Wiesbaden **1980**.
- [48] D. V. Schroeder, *An Introduction to Thermal Physics*, Addison Wesley Longman, San Francisco, CA **2005**.
- [49] F. Stadler, *Doctoral Thesis*, Ludwig-Maximilians-Universität, München, **2006**.
- [50] H. Lueken, *Magnetochemie: Eine Einführung in Theorie Und Anwendung*, Springer eBook Collection, Vieweg+Teubner Verlag, Wiesbaden **1999**.
- [51] N. F. Chilton, R. P. Anderson, L. D. Turner, A. Soncini, K. S. Murray, *J. Comput. Chem.* **2013**, 34 1164.